

Rethinking Causality-driven Robot Tool Segmentation with Temporal Constraints

Hao Ding^{1*}, Jie Ying Wu², Zhaoshuo Li¹ and Mathias Unberath^{1*}

^{1*}Department of Computer Science, Johns Hopkins University, 3400 N. Charles St, Baltimore, 21218, MD, USA.

²Department of Computer Science, Vanderbilt University, 2201 West End Ave, Nashville, 37235, TN, USA.

*Corresponding author(s). E-mail(s): hding15@jhu.edu; unberath@jhu.edu;

Abstract

Purpose: Vision-based robot tool segmentation plays a fundamental role in surgical robots and downstream tasks. CaRTS, based on a complementary causal model, has shown promising performance in unseen counterfactual surgical environments in the presence of smoke, blood, etc. However, CaRTS requires over 30 iterations of optimization to converge for a single image due to limited observability. **Method:** To address the above limitations, we take temporal relation into consideration and propose a temporal causal model for robot tool segmentation on video sequences. We design an architecture named Temporally Constrained CaRTS (TC-CaRTS). TC-CaRTS has three novel modules to complement CaRTS – temporal optimization pipeline, kinematics correction network, and spatial-temporal regularization. **Results:** Experiment results show that TC-CaRTS requires much fewer iterations to achieve the same or better performance as CaRTS. TC-CaRTS also has the same or better performance in different domains compared to CaRTS. All three modules are proven to be effective. **Conclusion:** We propose TC-CaRTS, which takes advantage of temporal constraints as additional observability. We show that TC-CaRTS outperforms prior work in the robot tool segmentation task with improved convergence speed on test datasets from different domains.

Keywords: Deep Learning, Computer Vision, Minimally invasive surgery, Computer-assisted surgery, Robustness

1 Introduction

With the widespread application of surgical robots and the growing demand for autonomous surgery, vision-based robot tool segmentation plays a fundamental role in robot perception [1–10]. In surgical scenes, performances and robustness of segmentation algorithms are both important aspects for the success and safety of downstream operations. Various feed-forward networks and machine-learning techniques designed for semantic/instance segmentation have achieved promising performance [11–18]. However, their performance does not generalize when tested on data from different domains [19]. To improve robustness, some effort has already been made [20–24]. CaRTS [24], designed from a complementary causal model, shows a promising and robust performance when tested on counterfactual surgical environments for robot tool segmentation. However, optimization from an image-wise perspective faces limited observability. This limitation makes CaRTS hard to optimize.

In order to alleviate this issue, we propose a temporal causal model which frames robot tool segmentation along a sequence. This temporal causal model is shown in Fig. 1. We use the same idea from CaRTS where images \mathbf{I}^t and segmentation \mathbf{S}^t at timestamp t are directly determined by all unobserved robot and camera parameters \mathbf{T}^t , and the environment \mathbf{E}^t at the same timestamp t . We assume occlusion has no effect on segmentation and there is no interaction between tools and environments. As the model describes, \mathbf{T}^{t+1} at timestamp $t + 1$ are directly determined by \mathbf{T}^t , \mathbf{T}^{t-1} , and all \mathbf{T} s in the past. Exploring this temporal causal effect might provide temporal constraints that are effective to deal with the issues mentioned above.

We explore the underlining temporal constraints in this temporal causal model. The first direction is to differentiate time-variant and time-invariant factors in \mathbf{T} and optimize them differently according to their property. Kinematics, with notation \mathbf{K} , is representative of time-variant factors. Modeling the causal effect of \mathbf{K} s by $P(\mathbf{K}^t | \mathbf{K}^{t-1}, \mathbf{K}^{t-2}, \dots)$ can be a promising direction since the model can learn motion property from the previous trajectory to provide constraints. Another direction for the time-variant factors is making the spatial-temporal smoothness assumption, which assumes the measurement error and the inter-frame motion is small. This assumption should be safe to make since the difference between two adjacent timestamps is small and the speed of the robot is limited. Inspired by these directions, we propose temporally constrained CaRTS (TC-CaRTS) architecture. TC-CaRTS has three novel modules upon CaRTS. The first is a temporal optimization pipeline that enables the optimization of time-invariant factors like base configuration. The second is a kinematics correction network (KCN) that models the temporal causal effect for kinematics. The third is a spatial-temporal regularization based on the spatial-temporal smoothness assumption.

Our experiments show that TC-CaRTS effectively reduced the required iterations to achieve the same or better segmentation performance compared to CaRTS. Ablation studies indicate this improvement comes from the temporal constraints utilized by all three proposed modules. The code will be released.

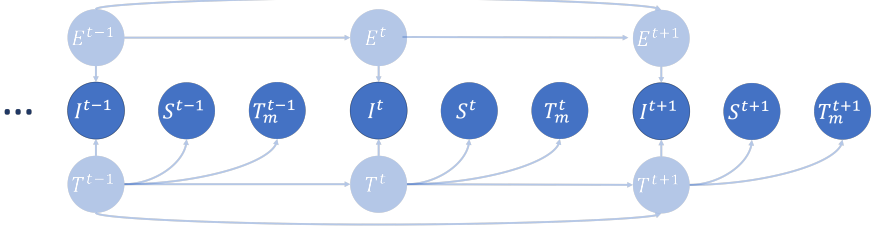


Fig. 1: Illustration of the temporal causal model for robot tool segmentation task. Arrow lines mean direct causal effect. At timestamp t , We note \mathbf{I}^t for image, \mathbf{E}^t for environment, \mathbf{S}^t for segmentation, \mathbf{T}^t for true robot kinematics and camera poses, \mathbf{T}_m^t for measured robot kinematics and camera poses

In summary, the main contributions of this paper are as follows: (1) Modeling temporal causal relations and exploring potential direction temporal constraints in this model. (2) Proposing TC-CaRTS that utilize the temporal constraints in (1) that requires fewer iterations to achieve the same or better performance compared to CaRTS.

2 Related Work

Robot Tool Segmentation:

Both image-wise and video-wise semantic or instance segmentation have already been a maturely-developed area. Feed-forward networks, e.g. [11–18], are on a dominating stand. Their variants [1–5, 7] are also the state-of-the-art on robot tool segmentation. At the same time, increasing efforts have been made to incorporate other available information, e.g. geometric information [25–27] and kinematics [8, 9], with visual input to improve performance [6, 8, 9] or robustness [10, 24] for robot tool segmentation.

Causality in Computer Vision:

Causality has been receiving increasing attention in computer vision research, especially medical area. Some researchers use ideas from causal inference to design feature representation learning methods [20–23] for domain generalization. Some researchers use the concept of counterfactual for generative models [28, 29]. Lenis et al. [30] use this concept for the interpretability of medical image classifiers. Some researchers focus on posing the underlying causal model of the vision task [24, 31].

CaRTS:

Ding et al. [24] have proposed a novel causal model where the segmentation is directly determined by the robot kinematics, camera poses, and the environment instead of the observed image. Based on this causal model they design CaRTS architecture that iteratively optimizes feature similarity between rendered images and observed images w.r.t the measured kinematics to estimate

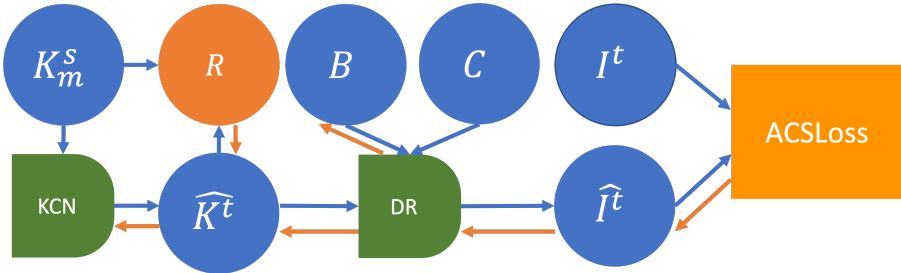


Fig. 2: Illustration of the overall architecture of TC-CaRTS. \mathbf{K}_m^s denotes the robot kinematics of a time segment $\mathbf{s} = \{t, t-1, \dots, t-n-1\}$. $\hat{\mathbf{K}}^t$ denotes corrected kinematics output by KCN. \mathbf{R} denotes spatial-temporal regularization term. \mathbf{B} denotes robot base configuration. \mathbf{C} denotes all other parameters that are required for rendering, e.g. camera configurations, mesh models, DH parameters, etc. \mathbf{I}^t and $\hat{\mathbf{I}}^t$ denotes observed and rendered image respectively. Solid blue lines in this figure represent information flow and solid orange lines represent gradient flow. DR stands for differentiable rendering.

true kinematics. The final segmentation is the rendered silhouette of the robot model given the estimated kinematics. CaRTS achieves outstanding robustness across testing domains compared to other feed-forward networks. However, limited observability in image-wise optimization makes CaRTS hard to achieve real-time inference. Our temporal causal model and TC-CaRTS architecture incorporate temporal constraints that are intuitively helpful for this limitation.

3 Method

We propose the TC-CaRTS architecture based on our temporal causal model. The basic modeling of TC-CaRTS is similar to CaRTS but has three novel modules. We introduce the temporal optimization pipeline first and then introduce KCN and spatial-temporal regularization.

3.1 Temporal Optimization Pipeline

The temporal optimization pipeline is illustrated in Fig.2. Notations are described in the caption of Fig.2. The optimization objective function in TC-CaRTS is the spatial-temporal regularized ACSLoss between deep feature maps extracted from the observed image \mathbf{I}^t and rendered image $\hat{\mathbf{I}}^t$. ACSLoss calculates an attentional cosine similarity between feature maps. CaRTS use pre-trained U-Net to extract feature maps from observed image and a hybrid image made up of rendered robot tool and the average background from the training dataset. Optimizing ACSLoss between these two feature maps aligns the calculated robot configuration to the observed robot. Since the robot tool is

differentially rendered, the gradient can be backpropagated to the input kinematics. Thus, gradient descent can be performed to correct the measurement error. More details about the optimization pipeline can be found in [24]

Different from the image-wise CaRTS pipeline, the temporal optimization pipeline differentiates the time-variant factor and time-invariant factor. In TC-CaRTS, time-variant means robot kinematics sequence \mathbf{K}_m^s and time-invariant factor means robot base configuration \mathbf{B} . Other factors \mathbf{C} remain constant during optimization. The optimization objective function can be written as Eq. 1 where θ is KCN’s weights.

$$\arg \min_{\theta, \mathbf{B}} ACSLoss(\widehat{\mathbf{K}}^t, \mathbf{B}, \mathbf{C}) + \mathbf{R} \quad (1)$$

During optimization, we alternatively perform gradient descent for θ and \mathbf{B} . At each timestamp t , we first calculate ACSLoss, backpropagate gradient, and perform gradient descent for θ in KCN for k iterations to learn the temporal relation of kinematics for KCN. Then, we freeze KCN and repeat the above optimization process for \mathbf{B} for one iteration. The final corrected kinematics $\widehat{\mathbf{K}}^t$, base configuration $\widehat{\mathbf{B}}$, and \mathbf{C} are used to render the predicted segmentation $\widehat{\mathbf{S}}^t$.

3.2 Kinematics Correction Network

The Kinematics Correction Network (KCN) is an MLP network F_θ . The input kinematics \mathbf{K}_m^s is a $n \times d$ matrix, d is the dimension of the kinematics, and n is the number of timestamps. $PE(n)$ is the positional encoding for each timestamp. The output is the corrected kinematics $\widehat{\mathbf{K}}^t$ that estimates the true kinematics. KCN can be expressed as Eq. 2:

$$\widehat{\mathbf{K}}^t = \mathbf{K}_m^s + F_\theta(\mathbf{K}_m^s + PE(n)) \quad (2)$$

3.3 Spatial-temporal Regularization

The spatial-temporal regularization is based on the spatial-temporal smoothness assumptions that (a) the measurement error is small and (b) the inter-frame motion between consecutive timestamps is small. As we use joint angles as kinematics to optimize, we use the L2 norm to regularize them. The Regularization term can be written as:

$$R = \lambda_1 \frac{1}{d} \sum_{i=1}^d (\widehat{\mathbf{K}}^{t,i} - \mathbf{K}^{t,i})^2 + \lambda_2 \frac{1}{d} \sum_{i=1}^d (\widehat{\mathbf{K}}^{t,i} - \widehat{\mathbf{K}}^{t-1,i})^2 \quad (3)$$

where i represents the dimension indices of the kinematics $\widehat{\mathbf{K}}^{t,i}$ calculated via Eq. 2. R denotes the whole regularization term, λ_1, λ_2 are hyperparameters for adjusting regularization strength of each term. $(\widehat{\mathbf{K}}^{t,i} - \mathbf{K}^{t,i})^2$ in the first term regularizes according to assumption (a) and $(\widehat{\mathbf{K}}^{t,i} - \widehat{\mathbf{K}}^{t-1,i})^2$ in the second term regularizes according to assumption (b).



Fig. 3: Example of the counterfactual images from different domains at the same timestamp

4 Experiment

We perform the robot tool segmentation experiment on the dataset from CaRTS[24]. The dataset has nine videos (seven for training, one for validation, and one for testing). Each video contains 400 frames. Each frame has its corresponding kinematics for both patient-side manipulators (PSMs). All videos were recorded under the same camera setting and robot base configuration which are roughly measured before recording. Robot motion recorded in all videos is in free space and no occlusion exists. We train the U-Net [11] feature extractors and all baseline models on the training dataset which only contains videos recorded from one domain without any corruption. We call this domain the regular domain. The validation and test dataset contain counterfactual videos that are recorded on other domains, e.g. smoke, bleeding, etc. Examples of the counterfactual image from different domains are shown in Fig. 3.

In our experiment, we use Dice as the metric for measuring segmentation performance. We first explore the inference speed improvement of our TC-CaRTS architecture compared to CaRTS on the test dataset. We also compare the performance of TC-CaRTS to other deep learning algorithms on the test dataset. Then we present ablation studies on the validation dataset.

4.1 Implementation Details

In our experiment, we use the same implementation setting from CaRTS. For KCN, we choose input length $n = 5$ and optimize all six joint angles and one tool angle of the two PSMs which makes the dimension of the kinematics $d = 14$, KCN has five hidden layers with 32, 64, 128, 128, 64, 32 channels. For spatial-temporal regularization we set $\lambda_1 = 10$ and $\lambda_2 = 1$. We use Adam optimizer with a learning rate of $5 \times 10^{-5} / 3 \times 10^{-6}$ for θ / \mathbf{B} . All baselines are trained for 50 epochs with smoke augmentation. All of the experiments run on a single NVIDIA GeForce RTX 3090 graphic card.

4.2 Speed Improvement

To measure speed improvement, we draw inference time vs performance plots for both CaRTS and TC-CaRTS when inferring with different iteration times k per frame. We choose $k = 1, 2, 3, 5, 10, 30, 50$ and test on the regular domain and bleeding domain. The quantitative results are in Tab. 1 and the corresponding plot is shown in Fig 4. From the results, both CaRTS and TC-CaRTS

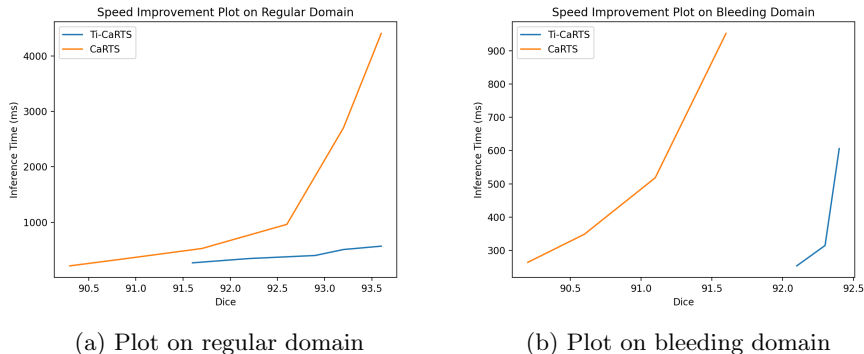


Fig. 4: Results of the speed improvement experiment

Table 1: Quantitative Results of the Speed Improvement

Regular	$k = 1$	3	5	10	30	50
CaRTS	90.3 ± 3.8	90.9 ± 3.8	91.7 ± 3.6	92.6 ± 3.2	93.2 ± 3.6	93.6 ± 2.9
inference time	213ms	345ms	526ms	961ms	2702ms	4405ms
TC-CaRTS	91.6 ± 3.9	93.2 ± 2.8	93.6 ± 2.7	93.6 ± 2.7	-	-
inference time	267ms	415ms	568ms	-	-	-
Bleeding	$k = 1$	3	5	10	30	50
CaRTS	90.2 ± 3.8	90.6 ± 3.7	91.1 ± 3.7	91.6 ± 4	91.6 ± 4	-
inference time	263ms	348ms	518ms	-	-	-
TC-CaRTS	92.1 ± 3.1	92.3 ± 3	92.4 ± 2.9	-	-	-
inference time	253ms	314ms	606ms	-	-	-

converge at a dice score of 93.6 on the regular domain while TC-CaRTS requires much fewer iterations (5 vs 50) than CaRTS. On the bleeding domain, TC-CaRTS after a single iteration outperformed CaRTS optimized with 10 iterations. Although TC-CaRTS is not real-time yet, it decreases the number of iterations for the optimization to converge. This is a significant step towards real-time inference.

4.3 Performance on Robot Tool Segmentation

In this experiment, we compare the tool’s Dice score of TC-CaRTS to CaRTS [24], image-based baselines including HRNet [17], Swin Transformer [16], and method by Colleoni et al [10] and a video-based baseline STCN [18]. All baselines are trained with simulated smoke augmentation. As Tab. 2 shows, all the feed-forward network-based methods perform well on the regular domain and they can achieve real-time inference. However, their performances deteriorate significantly in other domains that are unseen in the training dataset. TC-CaRTS retains comparable performance as CaRTS on all domains.

Table 2: Robot Tool Segmentation Results

	Regular	Low Brightness	Bleeding	Smoke	BG Change	FPS
Colleoni’s	94.9 \pm 2.7	87.0 \pm 4.5	55.0 \pm 5.7	59.7 \pm 24.7	75.1 \pm 3.6	35.8
HRNet	95.2 \pm 2.7	86.3 \pm 3.9	56.3 \pm 16.4	77.2 \pm 23.6	92.1 \pm 4.6	15.6
Swin Transformer	95.0 \pm 5.5	93.0 \pm 5.5	76.5 \pm 9.0	82.4 \pm 17.0	94.8 \pm 5.3	24.4
STCN	92.2 \pm 2.7	64.3 \pm 6.9	30.8 \pm 10.4	69.2 \pm 26.5	84.0 \pm 5.6	27.5
CaRTS	93.4 \pm 3.0	92.4 \pm 3.1	90.8 \pm 4.4	91.6 \pm 4.7	92.3 \pm 4.8	0.37
TC-CaRTS	93.6 \pm 2.7	92.3 \pm 3.3	92.2 \pm 3.3	91.9 \pm 4.5	92.5 \pm 3.1	1.76

Table 3: Results of the ablation study for the effectiveness of all modules

CaRTS	Ti Optim	KCN	ST Reg	$k = 1$	$k = 3$	$k = 5$	$k = 10$
✓				89.4 \pm 2.8	90.8 \pm 3.0	91.2 \pm 3.0	91.9 \pm 3.7
✓	✓			90.4 \pm 2.8	91.5 \pm 2.8	91.9 \pm 3.0	92.1 \pm 2.4
✓		✓		90.6 \pm 3.2	91.1 \pm 3.0	91.5 \pm 2.7	54.3 \pm 43.0
✓		✓	✓	91.1 \pm 2.9	91.9 \pm 2.6	92.2 \pm 2.9	92.4 \pm 2.7
✓	✓	✓	✓	91.4 \pm 3.1	92.5 \pm 2.6	92.7 \pm 2.6	92.8 \pm 2.4

Table 4: Results of the ablation study for input length

n	1	3	5	10	20	40
Dice	91.3 \pm 3.0	93.0 \pm 2.4	92.6 \pm 2.6	92.3 \pm 3.2	91.7 \pm 3.4	92.3 \pm 3.0

4.4 Ablation Study

We perform ablation studies on the regular domain of the validation dataset to explore the effectiveness of all modules and design choices.

Effectiveness of all modules:

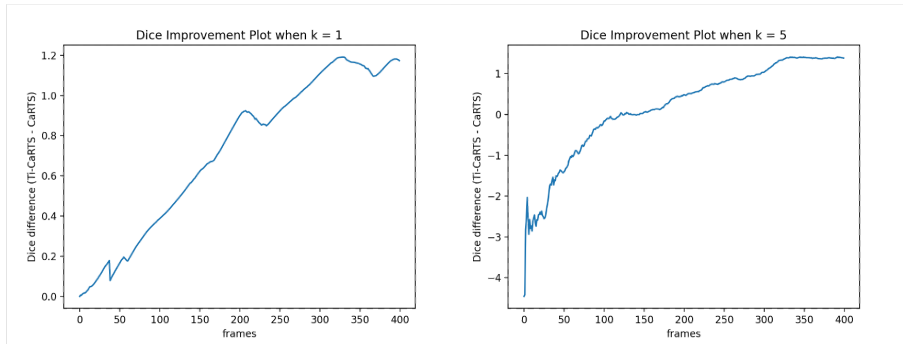
We explore the effectiveness of the modules by adding them to the CaRTS architecture. From Tab. 3, we find that using the temporal optimization pipeline can improve performance. Adding KCN can also improve performance when k is small. But when k becomes larger, it might overfit some frames and fail to generalize without spatial-temporal regularization which is shown as the result when $k = 10$. The spatial-temporal regularization not only improves the performance when k is small and accelerates the convergence but also stabilizes the optimization process of KCN for larger k .

Input Length:

We perform an ablation study to see the influence of the input length n for KCN. We test on $n = 1, 3, 5, 10, 40$. From Tab. 4 We find that if we only use the current frame, i.e. $n = 1$, there will be a limited improvement compared to CaRTS. Once previous frames are provided $n \geq 3$, the improvement becomes obvious. This indicates that the improvement comes from temporal constraints. However, with a further increase in the input length, the performance does not increase. We suppose this is because increasing the input length will also increase the difficulty of the optimization.

Table 5: Results of the ablation study for regularization strength

λ_1	0	1	10	100	1000	10000
Dice	91.1 ± 2.9	91.3 ± 3.0	92.6 ± 2.6	92.8 ± 2.7	91.2 ± 3.3	91.0 ± 3.0
λ_2	0	0.1	1	10	100	1000
Dice	92.1 ± 3.0	92.6 ± 2.6	92.6 ± 2.6	92.3 ± 3.0	91.1 ± 3.3	88.4 ± 3.5

**Fig. 5:** Dice improvement over frames***Regularization Strength:***

We perform an ablation study to see the influence of the regularization strength λ_1, λ_2 in the spatial-temporal regularization. We separately test on $\lambda_1 = 0, 1, 10, 100, 1000, 10000$ when $\lambda_2 = 1$ and $\lambda_2 = 0, 0.1, 1, 10, 100, 1000$ when $\lambda_1 = 10$. From Tab. 5 we find that when we set either λ_1 or λ_2 to 0, there are performance drops (1.5 / 0.5 dice score) compared to the default setting. When regularization is too strong ($\lambda_1 \geq 1000, \lambda_2 \geq 100$), optimization might also become harder.

Effectiveness over time:

We perform an ablation study to show an insight into the TC-CaRTS’s effectiveness over time. We calculate the average Dice difference of the first m frames for $m = 1, 2, \dots, 400$ between TC-CaRTS and CaRTS. The result plots are shown in Fig. 5. As the plots show, the Dice difference increases as m increases. This indicates that with more temporal information having been processed, TC-CaRTS’s advantage with temporal constraints becomes more obvious. We also find that when m is small (≤ 50), TC-CaRTS performs worse than CaRTS when $k = 5$. This indicates that TC-CaRTS might overfit some early frames. However, when more m increases, TC-CaRTS start to outperform CaRTS.

5 Limitations

Although TC-CaRTS is proven to be effective. There are still limitations that are not fully resolved. Firstly, the challenge to achieve real-time remains. On

the one hand, differentiable rendering and backpropagation require more computation than a single feed-forward network. On the other hand, redundant feature extraction operations on similar rendered images also restrict the inference speed. Secondly, the architecture works under the assumption that there is no occlusion and interaction. To deal with occlusion and interaction, information for the environmental factor \mathbf{E} is necessary. The representation of \mathbf{E} might be estimated through vision or other sensors. All of these limitations also imply essential directions for future work.

6 Conclusion

In summary, limited observability causes slow convergence for CaRTS. We propose a temporal causal model and explore underlying temporal constraints in this model. Inspired by the temporal causal model, we propose TC-CaRTS with three novel modules to complement CaRTS—temporal optimization pipeline, kinematics correction network, and spatial-temporal regularization. TC-CaRTS requires fewer iterations to achieve the same or better performance as CaRTS while achieving the same or better performance in different domains compared to CaRTS. Ablation studies indicate that all modules are effective and the effectiveness comes from temporal constraints.

Acknowledgement:

This research is supported by a collaborative research agreement with the MultiScale Medical Robotics Center at The Chinese University of Hong Kong.

References

- [1] et al., L.C.G.: Toolnet: Holistically-nested real-time segmentation of robotic surgical tools. In: Proc. IROS (2017)
- [2] Jin, Y., Cheng, K., Dou, Q., Heng, P.: Incorporating temporal prior from motion flow for instrument segmentation in minimally invasive surgery video. In: Proc. MICCAI (2019)
- [3] Shvets, A.A., Rakhlin, A., Kalinin, A.A., Iglovikov, V.I.: Automatic instrument segmentation in robot-assisted surgery using deep learning. In: Proc. ICMLA (2018)
- [4] Pakhomov, D., Premachandran, V., Allan, M., Azizian, M., Navab, N.: Deep residual learning for instrument segmentation in robotic surgery. In: Proc. MLMI (2019)
- [5] Islam, M., Atputharuban, D.A., Ramesh, R., Ren, H.: Real-time instrument segmentation in robotic surgery using auxiliary supervised deep adversarial learning. IEEE Robotics and Automation Letters (2019)

- [6] Qin, F.e.a.: Surgical instrument segmentation for endoscopic vision with data fusion of cnn prediction and kinematic pose. In: Proc. ICRA (2019)
- [7] Zhao, Z., Jin, Y., Lu, B., Ng, C., Dou, Q., Liu, Y., Heng, P.: One to many: Adaptive instrument segmentation via meta learning and dynamic online adaptation in robotic surgical video. In: Proc. ICRA (2021)
- [8] Su, Y.-H., Huang, K., Hannaford, B.: Real-time vision-based surgical tool segmentation with robot kinematics prior. In: 2018 International Symposium on Medical Robotics (ISMR), pp. 1–6 (2018). IEEE
- [9] da Costa Rocha, C., Padoy, N., Rosa, B.: Self-supervised surgical tool segmentation using kinematic information. In: 2019 International Conference on Robotics and Automation (ICRA), pp. 8720–8726 (2019). IEEE
- [10] Colleoni, E., Edwards, P.J., Stoyanov, D.: Synthetic and real inputs for tool segmentation in robotic surgery. In: Proc. MICCAI (2020)
- [11] Ronneberger, O., Fischer, P., Brox, T.: U-net: Convolutional networks for biomedical image segmentation. In: Proc. MICCAI (2015)
- [12] Chen, L., Zhu, Y., Papandreou, G., Schroff, F., Adam, H.: Encoder-decoder with atrous separable convolution for semantic image segmentation. In: Proc. ECCV (2018)
- [13] He, K., Gkioxari, G., Dollár, P., Girshick, R.B.: Mask R-CNN. In: Proc. ICCV (2017)
- [14] Chen, K., Pang, J., Wang, J., Xiong, Y., Li, X., Sun, S., Feng, W., Liu, Z., Shi, J., Ouyang, W., Loy, C.C., Lin, D.: Hybrid task cascade for instance segmentation. In: Proc. CVPR (2019)
- [15] Ding, H., Qiao, S., Yuille, A.L., Shen, W.: Deeply shape-guided cascade for instance segmentation. In: Proc. CVPR (2021)
- [16] Liu, Z., Lin, Y., Cao, Y., Hu, H., Wei, Y., Zhang, Z., Lin, S., Guo, B.: Swin transformer: Hierarchical vision transformer using shifted windows. In: Proc. ICCV (2021)
- [17] Wang, J., Sun, K., Cheng, T., Jiang, B., Deng, C., Zhao, Y., Liu, D., Mu, Y., Tan, M., Wang, X., Liu, W., Xiao, B.: Deep high-resolution representation learning for visual recognition. TPAMI (2019)
- [18] Cheng, H.K., Tai, Y.-W., Tang, C.-K.: Rethinking space-time networks with improved memory coverage for efficient video object segmentation. In: NeurIPS (2021)
- [19] Drenkow, N., Sani, N., Shpitser, I., Unberath, M.: Robustness in deep

- learning for computer vision: Mind the gap? arxiv:2112.00639 (2021)
- [20] Mitrovic, J., McWilliams, B., Walker, J.C., Buesing, L.H., Blundell, C.: Representation learning via invariant causal mechanisms. In: Proc. ICLR (2021)
- [21] Ouyang, C., Chen, C., Li, S., Li, Z., Qin, C., Bai, W., Rueckert, D.: Causality-inspired single-source domain generalization for medical image segmentation. arxiv:2111.12525 (2021)
- [22] Zhang, C., Zhang, K., Li, Y.: A causal view on robustness of neural networks. In: Larochelle, H., Ranzato, M., Hadsell, R., Balcan, M., Lin, H. (eds.) Proc. NIPS (2020)
- [23] Liu, C., Sun, X., Wang, J., Tang, H., Li, T., Qin, T., Chen, W., Liu, T.-Y.: Learning causal semantic representation for out-of-distribution prediction. Proc. NIPS (2021)
- [24] Ding, H., Zhang, J., Kazanzides, P., Wu, J.Y., Unberath, M.: Carts: Causality-driven robot tool segmentation from vision and kinematics data. In: Proc. MICCAI, pp. 387–398 (2022). Springer
- [25] Allan, M., Ourselin, S., Hawkes, D.J., Kelly, J.D., Stoyanov, D.: 3-d pose estimation of articulated instruments in robotic minimally invasive surgery. IEEE Trans. Medical Imaging (2018)
- [26] Li, Z., Liu, X., Drenkow, N., Ding, A.S., Creighton, F.X., Taylor, R.H., Unberath, M.: Revisiting stereo depth estimation from a sequence-to-sequence perspective with transformers. In: Proc. ICCV (2021)
- [27] Ye, M., Zhang, L., Giannarou, S., Yang, G.: Real-time 3d tracking of articulated tools for robotic surgery. In: Proc. MICCAI (2016)
- [28] Reinhold, J.C., Carass, A., Prince, J.L.: A structural causal model for MR images of multiple sclerosis. In: Proc. MICCAI (2021)
- [29] Pawlowski, N., de Castro, D.C., Glocker, B.: Deep structural causal models for tractable counterfactual inference. In: Proc. NIPS (2020)
- [30] Lenis, D., Major, D., Wimmer, M., Berg, A., Sluiter, G., Bühler, K.: Domain aware medical image classifier interpretation by counterfactual impact analysis. In: Proc. MICCAI (2020)
- [31] Castro, D.C., Walker, I., Glocker, B.: Causality matters in medical imaging. Nature Communications (2020)